Since January 2020 Elsevier has created a COVID-19 resource centre with free information in English and Mandarin on the novel coronavirus COVID-19. The COVID-19 resource centre is hosted on Elsevier Connect, the company's public news and information website.

Sensors & Actuators: B. Chemical 383 (2023) 133575

Contents lists available at ScienceDirect

Sensors and Actuators: B. Chemical

journal homepage: www.elsevier.com/locate/snb

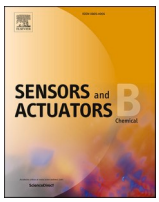

Sensitivity-enhanced nanoplasmonic biosensor using direct immobilization of two engineered nanobodies for SARS-CoV-2 spike receptor-binding domain detection

Zhengtai Ma [a,b], Zengchao Sun [c], Xiaoqing Lv [a], Hongda Chen [a], Yong Geng [c,*], Zhaoxin Geng [d,*]

[a] State Key Laboratory for Integrated Optoelectronics, Institute of Semiconductors, Chinese Academy of Sciences, Beijing, China
[b] College of Materials Science and Opto-Electronic Technology, University of Chinese Academy of Sciences, Beijing, China
[c] The Chinese Academy of Sciences Key Laboratory of Receptor Research, State Key Laboratory of Drug Research, Shanghai Institute of Materia Medica, Chinese Academy of Sciences, Shanghai, China
[d] School of Information Engineering, Minzu University of China, Beijing, China

ARTICLE INFO

Keywords:
Nanoplasmonics
Biosensor
COVID-19
Nanobody
Immobilization
High-throughput

ABSTRACT

Sensitive, rapid, and easy-to-implement biosensors are critical in responding to highly contagious and fast-spreading severe acute respiratory syndrome coronavirus (SARS-CoV-2) mutations, enabling early infection screening for appropriate isolation and treatment measures to prevent the spread of the virus. Based on the sensing principle of localized surface plasmon resonance (LSPR) and nanobody immunological techniques, an enhanced sensitivity nanoplasmonic biosensor was developed to quantify the SARS-CoV-2 spike receptor-binding domain (RBD) in serum within 30 min. The lowest concentration in the linear range can be detected down to 0.01 ng/mL by direct immobilization of two engineered nanobodies. Both the sensor fabrication process and immune strategy are facile and inexpensive, with the potential for large-scale application. The designed nanoplasmonic biosensor achieved excellent specificity and sensitivity for SARS-CoV-2 spike RBD, providing a potential option for accurate early screening of the novel coronavirus disease 2019 (COVID-19).

1. Introduction

The novel coronavirus disease 2019 (COVID-19) caused by severe acute respiratory syndrome coronavirus (SARS-CoV-2) has caused a global pandemic due to large number of asymptomatic patients, long incubation period, and high transmission rate, seriously threatening human health and the global economy [1–5]. SARS-CoV-2 is still mutating, and the mutations are becoming more infectious [6–8]. There is an urgent need for sensitive, accurate, fast, simple, accessible, and inexpensive diagnostic tools to enable the early screening of infected persons to take appropriate isolation and treatment measures to prevent the spread of the virus.

The currently preferred diagnostic method for COVID-19 relies on detecting SARS-CoV-2 viral genetic material from the respiratory tract via reverse transcription polymerase chain reaction (RT-PCR), which offers high sensitivity and reliability [9,10]. However, it typically takes 5–6 h to complete with highly qualified personnel strictly controlling the risk of infection [11,12]. Immunoglobulin M (IgM)/immunoglobulin G (IgG) rapid test kits provide instant self-testing; however, their sensitivity and reliability have not reached the level of genomic molecule tests [13,14]. Detection of antibodies in serum allows for serological and immunological testing. However, this technique is not suitable for screening early and asymptomatic infected individuals because most infected individuals develop antibody responses approximately seven days after symptom onset [15–17]. Advanced nanotechnology-based biosensors based on nanomaterials and metal–organic frameworks can play an active role in COVID-19 diagnosis and virus infection control [18,19]. Localized surface plasmon resonance (LSPR) technology can realize highly sensitive, label-free, and easily accessible biosensing through refractive index (RI) changes generated by binding biomolecules around metal nanostructures [20,21]. The receptor-binding domain (RBD) of the SARS-CoV-2 spike protein is a highly specific target and is suitable for identifying Alpha, Beta, and Gamma variants [11,22]. Therefore, low-cost, convenient, and highly sensitive LSPR technology that directly detects viral antigens will be of great significance for the early large-scale and accurate diagnosis of COVID-19.

* Corresponding authors.
E-mail addresses: gengyong@simm.ac.cn (Y. Geng), zxgeng@muc.edu.cn (Z. Geng).

https://doi.org/10.1016/j.snb.2023.133575
Received 6 September 2022; Received in revised form 19 February 2023; Accepted 23 February 2023
Available online 24 February 2023

Funari et al. were the first to use an opto-microfluidic sensing platform of electrodeposited Au nanospikes to detect SARS-CoV-2 spike protein-specific antibodies in human plasma [23]. Huang et al. achieved fast, high-throughput quantification of SARS-CoV-2 neutralizing antibodies using nanoporous hollow Au nanoparticles (NPs) with enhanced coupling [24]. In current LSPR research, standard sensor chips usually use reagents such as thiols and sialylation to assist in the immobilization of antibodies, which complicates the functionalization process and increases the effect of biological functionalization operations on the results. Second, most of the current fabrication methods of nanostructures cannot achieve both low-cost and large-area uniform fabrication for higher-sensitivity fabrication of nanoplasmonic biosensors.

In this study, we developed a sensitivity-enhanced nanoplasmonic biosensor based on the direct immobilization of mixed nanobodies (NBs) to detect SARS-CoV-2 spike RBD. NBs are attractive alternatives to antibodies because of their higher solubility, stability, affinity, and selectivity [25–27]. In particular, they can be highly expressed in prokaryotic systems and easily engineered [28–30]. By modifying the linker with the amino acid sequence of GGGSC at the C-terminus of the NBs, the NBs can be immobilized directly, stably, and directionally, further simplifying the functionalization steps. Metal nanostructures were fabricated on a fluorine-doped tin oxide (FTO) substrate using a straightforward method of Au evaporation-annealing. The highest sensor sensitivity was obtained by optimizing the fabrication process conditions. The biosensor that directly immobilized the mixed NBs had a lower k value than the biosensor that immobilized any NB, which further improved the detection sensitivity of the SARS-CoV-2 spike RBD. Meanwhile, 36 biosensor chips were functionalized simultaneously in a homemade 36-well plate to obtain the detection results. Our work successfully demonstrated for the first time that a nanoplasmonic biosensor can directly immobilize two engineered NBs to detect SARS-CoV-2 spike RBD in serum with high sensitivity and specificity, which has great potential in the early direct and sensitive screening of COVID-19 infection.

2. Materials and methods

2.1. Materials and chemicals

Sucrose (S8271), sterile deionized water (F0020), His-tag antibody (K009795M), DYKDDDDK Tag antibody (K00972P), bovine serum albumin (BSA, SW3015), immunoglobulin G (IgG, SP001), and fetal bovine serum (FBS, S9020) were purchased from Solarbio. 6-Hydroxy-1-hexanethiol (MCH) was purchased from Sigma-Aldrich (product number: 451088). Phosphate buffered saline (PBS) was purchased from Hyclone (product number: SH30256.01). Alpha-fetoprotein (AFP; 30-AA06), carcinoembryonic antigen (CEA; 30-AC30), and cancer antigen 15–3 (CA15–3; 30 C-CP9064U) were obtained from Fitzgerald. The SARS-CoV-2 spike RBD, NB1D6, and NB4E9 were expressed and purified by the Shanghai Institute of Materia Medica, Chinese Academy of Sciences.

2.2. Preparation of Au NPs

By adjusting the thickness of the deposited Au, annealing temperature, and time, the Au evaporation-annealing process also provides excellent flexibility in preparing Au NPs for various biosensors. We first deposited Au on FTO substrates with thicknesses of 5 and 8 nm. We varied annealing temperature and time for Au deposited substrates using a combination of 50, 100, 150, 200, 250, 300 ℃ and 10, 30, and 60 min, respectively. As the 5 nm Au deposited substrates annealing treated at 300 ℃ for 30 min had the best optical properties of Au NPs, this condition was used for all characterization and application experiments. Fig. S1 shows the preparation and storage of the Au NP-covered substrate.

2.3. Functionalization of Au NPs

Fig. 1 shows a schematic illustration of the sensing mechanism strategy for the quantification of the SARS-CoV-2 spike RBD. NBs with high affinity and specificity for the SARS-CoV-2 spike RBD were directly immobilized on the surface of the Au NPs. The screening and preparation process of NBs includes the construction of a camelid NB phage-display library, screening and identification of NBs using phage-display technology, and expression and purification of NBs. The screening and preparation methods of NB1D6 and NB4E9 were consistent with the preparation methods for other NBs in the literature [27]. See Supplementary Material 4 for the complementary-determining region (CDR) sequences and size exclusion chromatography (SEC) profiles of NB1D6 and NB4E9. The related animal research work was approved and supervised by the Shanghai Institute of Materia Medica, Chinese Academy of Sciences (permit number: SYXK 2015–0027). After self-assembly of NBs on the surface of the Au NPs, the exposed free surface of the Au NPs was blocked by BSA. The detection target SARS-CoV-2 spike RBD was captured on the chip by specifically binding to the NBs. Before and after the combination of the SARS-CoV-2 spike RBD, the difference in the spectral elimination signal was obtained through the self-assembled LSPR optical platform.

NB1D6 and NB4E9 modified the linker with the amino acid sequence of GGGSC at the C-terminus of the NBs. The sulfhydryl group on cysteine can be directly fixed on the Au NP- covered substrate by forming an Au–S bond with Au NPs to form a self-assembled monolayer. Namely, Au NP-covered substrates were placed in a homemade 36-well plate containing 10 μg/mL of NBs (20 mM Tris, 100 mM NaCl, Tris-NaCl buffer pH 8.0) and stored overnight in a refrigerator at 4 °C. After successively rinsing with Tris-NaCl buffer and sterile deionized water, the substrate of the self-assembled NB was exposed to 1% BSA in a refrigerator at 4 °C for 2 h and block the remaining free surface to prevent non-specific adsorption. After rinsing with Tris-NaCl buffer followed by sterile deionized water, the immune substrate was stored at 4 °C until further use.

2.4. Measurement of SARS-CoV-2 Spike RBD using the homemade 36-well plate

The SARS-CoV-2 spike RBD stock solution was diluted in different proportions to prepare SARS-CoV-2 spike RBD Tris-NaCl solutions with gradient concentrations ranging from 0.01 to 10,000 ng/mL. FBS was used to simulate the serum environment of clinical samples to further verify the clinical application potential of the sensor chip. Serum samples were prepared by diluting the SARS-CoV-2 spike RBD stock solution in the FBS buffer at different ratios. The concentration of SARS-CoV-2 spike RBD was diluted with FBS to 1, 25, 100, and 1000 ng/mL to obtain simulated serum samples with gradient concentrations for comparison with corrected curves. Immune substrates were placed in homemade 36-well plates containing 50 μL of SARS-CoV-2 spike RBD Tris-NaCl solutions at different concentrations and incubated for 30 min at room temperature. After immune recognition, the immune substrates were rinsed with Tris-NaCl buffer and then sterile deionized water in turn.

2.5. Instrument

The LSPR optical platform was self-assembled in the laboratory (Fig. S2). The LSPR extinction spectra were obtained using a spectrometer (QE65000, Ocean Optics, USA). Scanning electron microscopy (SEM) images were obtained using aby field emission scanning electron microscope (NanoSEM650, FEI, USA). Fluorescence images were obtained using an optical microscope (Ti-s, Nikon, Japan).

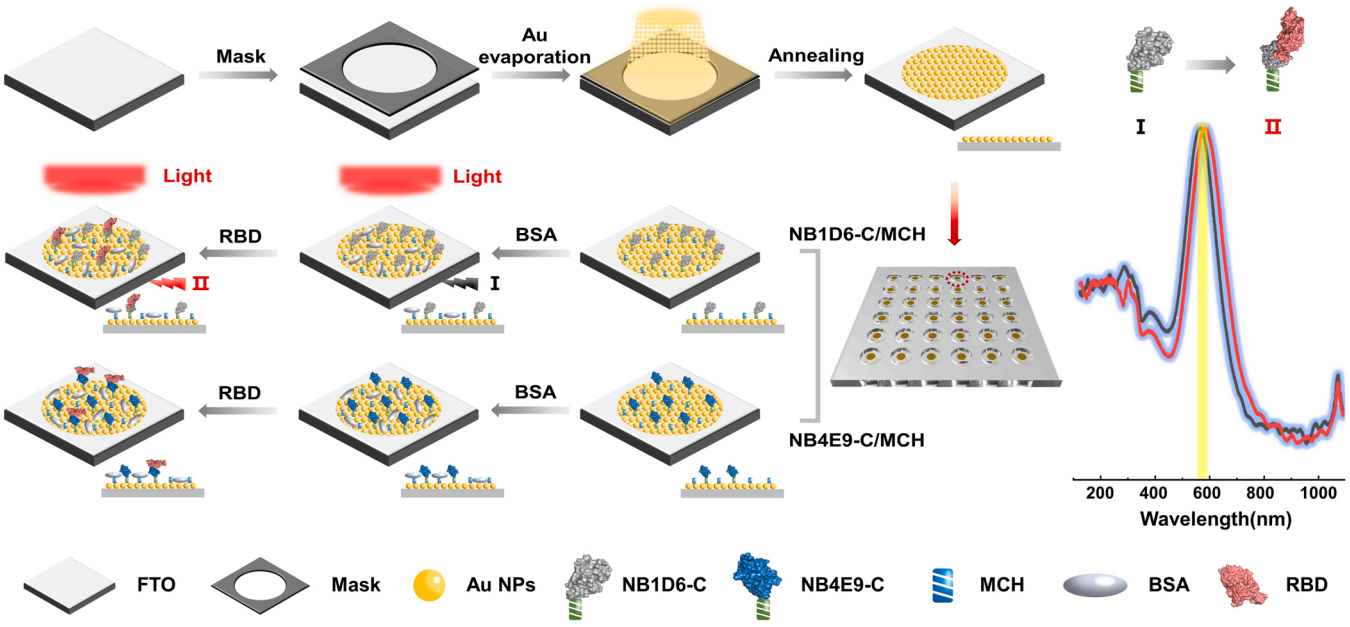

Fig. 1. Schematic illustration of nanoplasmonic biosensor for quantification of SARS-CoV-2 spike RBD.

3. Results and discussion

3.1. Morphological and optical properties of Au NPs

The stability and optical properties of Au NPs are crucial for LSPR immune sensing. As shown in Fig. 1, Au NPs for LSPR sensing were fabricated using the Au evaporation-annealing process. When metal NPs are deposited on glass substrates covered with indium tin oxide (ITO) or FTO film instead of commonly used glass substrates, the metal particles are embedded in the substrate during annealing to achieve more stable

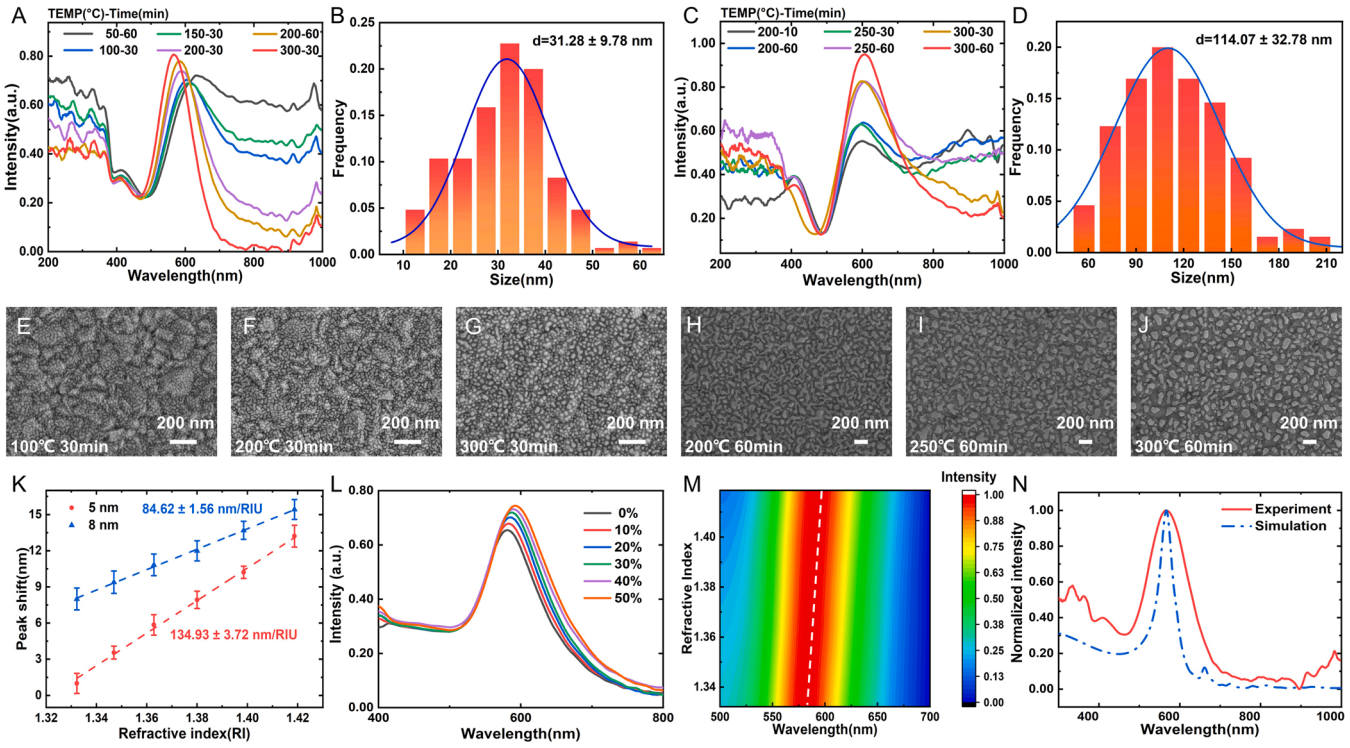

Fig. 2. Morphological characterization, optical properties, and sensing potential of Au NPs on FTO substrates. (A) Post-annealing spectra of FTO substrates deposited with 5 nm Au at different temperature and time conditions. (B) The particle size distribution of FTO substrates deposited with 5 nm Au under annealing conditions for optimal optical properties. (C) Post-annealing spectra of FTO substrates deposited with 8 nm Au at different temperature and time conditions. (D) The particle size distribution of FTO substrates deposited with 8 nm Au under annealing conditions for optimal optical properties. SEM images of FTO substrates deposited 5 nm Au (E–G) and 8 nm Au (H–I) under different temperature and time conditions. (K) LSPR spectral peak wavelengths are generated by exposure of the deposited 5 nm (red) and 8 nm (blue) substrates to different concentrations sucrose solutions. Spectra (L) and contour plots (M) of 5 nm Au deposited substrates exposed to different concentrations sucrose solutions. (N) The normalized experimental spectrum and the normalized simulated spectrum.

Au nanostructures [31,32]. Fig. 2A and C show the spectra of Au-deposited FTO substrates with thicknesses of 5 and 8 nm at different annealing temperatures and annealing times according to the adjustable parameters of the electron beam evaporation stage under the condition that the Au does not form a film on the FTO substrate. Fig. 2E–G shows the SEM images of the Au nanostructure formed on the substrate deposited with 5 nm Au under increasing annealing temperature. Combined with the spectrogram and morphology, the particle spacing of deposited Au gradually increases, and the particle size gradually decreases as the annealing temperature increases to 100, 200, and 300 °C.

According to Mie's theory [33], the calculation formula of the LSPR spectrum is as follows:

$$E(\lambda) = \frac{24\pi^2 N a^3 \varepsilon_m^{3/2}}{\lambda \ln(10)} \left[\frac{\varepsilon_i}{(\varepsilon_r - \chi\varepsilon_m)^2 + \varepsilon_i^2} \right]$$

where χ is the shape factor, and ε_m, ε_r, and ε_i are the external permittivity, the real, and the imaginary parts of the metal permittivity, respectively. The size of the NPs (a) is closely related to the resonance peak wavelength. During the annealing process, the absorption intensity at the off-resonance peak position gradually decreased with a change in particle size. The substrate deposited 5 nm Au will obtain the highest resonant intensity under the annealing condition of 300 °C for 30 min. At this time, the particle size tended to be the median value of the normal distribution. As shown in the size distribution figure (Fig. 2B), the particle size was 31.28 ± 9.78 nm. Fig. 2H–J shows the SEM images of the Au nanostructure formed on the substrate deposited with 8 nm Au with increasing annealing temperature. The morphological changes were consistent with the trend of the substrates deposited with 5 nm Au. The substrate deposited at 8 nm had the highest resonance strength after annealing at 300 °C for 60 min, and the particle size shown in Fig. 2D was 114.07 ± 32.78 nm.

The RI sensitivity of the biosensor, which is a critical parameter of the biosensor, can be measured by the peak wavelength shift of different RIs. Specifically, the Au NP-covered substrate was exposed to different concentrations of sucrose solution as the RI solution to change the ambient RI. The relationship between the LSPR peak and solution RI is shown in Fig. 2K. By calculation, the RI sensitivity of substrate deposited 5 nm Au is 134.93 nm/RIU, which is better than 84.62 nm/RIU of substrate deposited 8 nm Au under the annealing condition of optimal resonance strength. Therefore, a substrate deposited with 5 nm Au produces the best conditions to obtain the highest sensitivity, and the associated spectrum is shown in Fig. 2L. The spectral contour map (Fig. 2M) clearly shows the spectral red-shift of the Au NP- covered substrate with increasing ambient RI sensitivity. The finite difference time domain (FDTD) spectrum simulation of Au NPs based on the 31.28 nm result shown in the particle size distribution diagram is consistent with the peak position of the actual spectrum (Fig. 2N). The simulation model is illustrated in Fig. S3. The larger half-height width of the experimental spectrum was mainly due to the spectral influence of other NPs with various particle sizes. Compared with the RI sensitivity of Au nanostructures reported in the current literature [34–36], although this preparation method does not have the highest RI sensitivity, the convenient and inexpensive preparation process means this technique has great potential for large-scale production.

3.2. Direct immobilization of NBs

NBs are the recombinant minimal antigen-recognizing domains of heavy-chain-only antibodies produced by camels and Llamas [37,38]. The advantage of NBs as a good alternative to antibodies lies in their suitability for modification and potential for direct immobilization. However, the standard immobilization of NBs is achieved by coupling the self-assembled surface of chemical reagents with the labeling of other amino acids [39,40]. Recently, Simões reported directly immobilizing NBs with cysteine on the surface of an Au film [41]. NB1D6 and NB4E9 have a high affinity for the spike glycoprotein on the surface of SARS-CoV-2 (Fig. 3A and Table S1). AlphaFold2 software, based on the neural network method, makes protein structure predictions with high accuracy [42,43]. In the preparation of NB1D6 and NB4E9, the sequence of NBs was obtained using phage display technology. The crystal structure of the NB was predicted based on the protein sequence of the input NB, as shown in Fig. 3B. SEC analysis showed that the purified NB1D6 and NB4E9 were monomers (Fig. S4). NB1D6 and NB4E9 can simultaneously bind to the RBD, indicative of three non-overlapping epitopes (Fig. 3C).

To further reduce the steric hindrance between the directly immobilized NBs, well-directed exposure, and SARS-CoV-2 spike RBD, the amino acid sequence of Gly–Gly–Gly–Ser–Cys was modified at the C-terminus of the NBs (Fig. 3D). MCH, with a length similar to that of the Gly–Gly–Gly–Ser–Cys sequence, was simultaneously self-assembled on the Au NP- covered substrate. The concentration of the immobilized NB was 10 μg/mL, and the concentration of MCH was gradually increased to 0, 2, 20, 100, 200, and 2000 μM. The response of NB1D6-C to 1 μg/mL SARS-CoV-2 spike RBD is shown in Fig. 3E. In stage I, the NBs self-assembled on the Au NP- covered substrate in disorder. When MCH is modified simultaneously (stage II), it can reduce the steric hindrance of NB self-assembly and expose more binding sites that shift the response peak. As the MCH concentration gradually increased, the positive effect of MCH on the directional modification of NBs gradually increased, reaching a stable maximum response in stage III. When the MCH concentration was further increased in stage IV, MCH accounted for a larger proportion of the surface of the Au NP- covered substrate, resulting in a decrease in the LSPR peak wavelength shift (Fig. 3G). As shown in Fig. 3F, the response of NB4E9-C to 1 μg/mL SARS-CoV-2 spike RBD also showed a consistent trend. Therefore, the optimal concentration of MCH used for subsequent immune assays was 100 μM. The proposed immunoassay protocol is validated in Section 3.3.

3.3. Characterization of functionalized substrates

Immunofluorescence often utilizes antibody–antigen specific binding to detect or examine responding antigens to validate biofunctionalization and immunoassay protocols. NB4E9-C has a His-tag, and His-tag antibody (Ab-F1) conjugated CoraLite 488 was selected to verify its self-assembly on the Au NP- covered substrate. The SARS-CoV-2 spike RBD has a Flag-tag, and the DYKDDDDK Tag antibody (Ab-F2) was conjugated with CoraLite 488 to verify its immunoassay on immune substrates. The supplementary material provides more details on the immunofluorescence modification experiments. Overall, the immunoassay protocol presented here mainly consists of two key stages: NB self-assembly and specific capture of the SARS-CoV-2 spike RBD. The Au NP-covered substrates were incubated with Ab-F1 after self-assembly of NB4E9-C. The fluorescence image is shown in Fig. 4B and the corresponding spectrum is shown in Fig. 4D. The fluorescence intensity increased dramatically from 4.94 to 62.81 after incubation with Ab-F1. The LSPR wavelength shifted 15.53 nm after the self-assembly of the NB and 3.44 nm after the adsorption of the fluorescent antibody. The immunofluorescence results were consistent with the spectral results, indicating that the NBs successfully self-assembled on the surface of the Au NPs. The Au NPs that realized the self-assembly of the NB1D6-C were incubated with RBD, Ab-F2, and Ab-F2 after RBD, as shown in Fig. 4E. No obvious fluorescence was observed after incubation with RBD or Ab-F2. In contrast, Ab-F2 after RBD incubation produced obvious fluorescence. The spectrogram showed that the wavelength shift occurred from the self-assembly of NBs to the incubation of the RBD, followed by incubation with fluorescent antibodies. This indicates that no substance can generate fluorescence from the self-assembly of the NB during the RBD incubation. The NB did not bind directly to the fluorescent antibody to generate fluorescence. Ab-F2 incubation following NB self-assembly and re-incubation of the RBD produced fluorescence from the specifically captured Ab-F2. The Au NPs of self-assembled NBs also bind to the

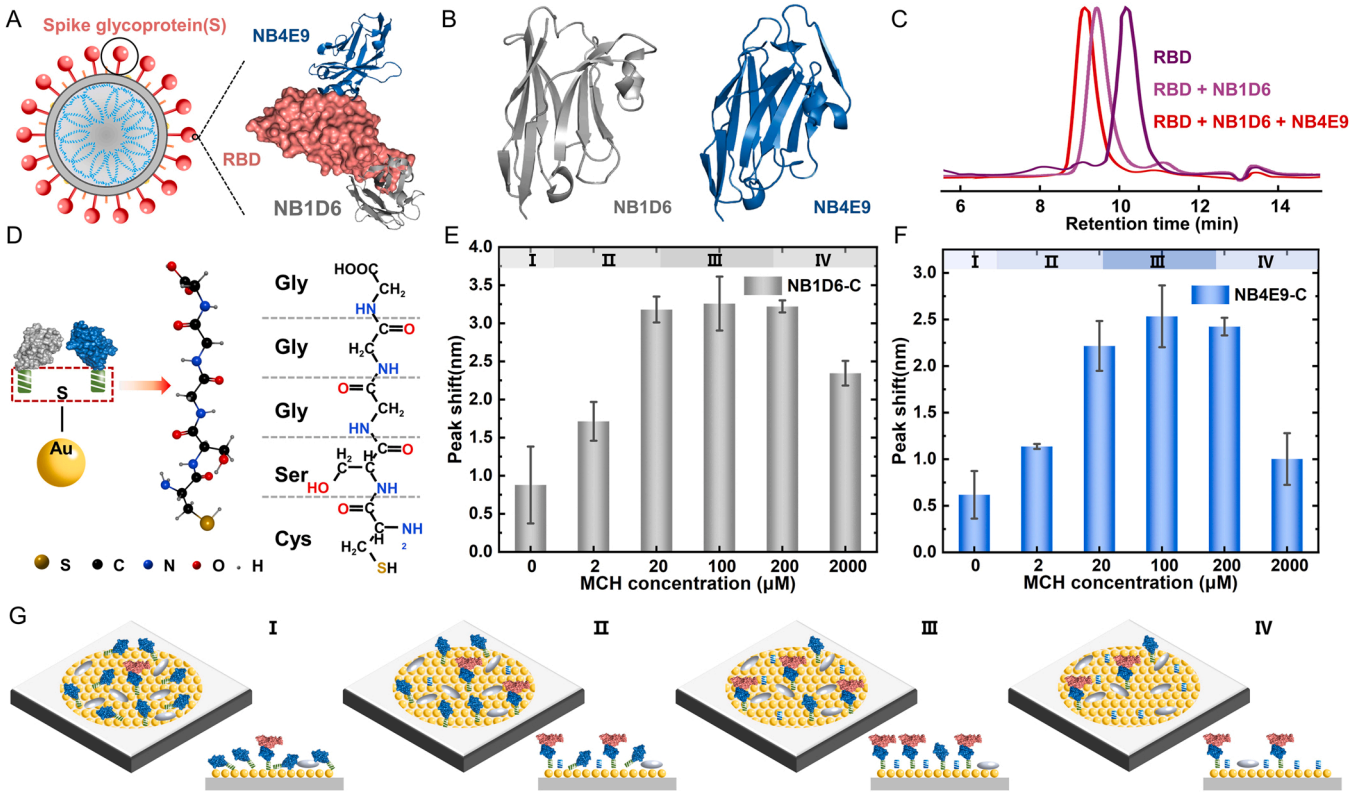

Fig. 3. Engineering and direct immobilization of nanobodies. (A) SARS-CoV-2 virus structure and details of NB1D6 and NB4E9 binding to RBD. (B) Structure of NB1D6 and NB4E9 predicted by AlphaFold2, with NB1D6 colored in gray and NB4E9 colored in blue, respectively. (C) Analysis of NB binding epitopes was performed using SEC. (D) Schematic illustration of the strategy for direct immobilization of NBs on Au NP-covered substrate. Wavelength shift of 1 μg/mL SARS-CoV-2 spike RBD of immune substrates prepared under the conditions of MCH concentrations of 0, 2, 20, 100, 200, and 2000 μM in direct immobilized NB1D6-C (E) and NB4E9-C (F) solution, respectively. (G) Schematic illustration of the self-assembly of NBs and MCH on Au NPs covered substrates under four stages (I, II, III, and IV).

SARS-CoV-2 spike RBD, which can specifically bind to Ab-F2. The NB4E9-C self-assembled on the surface of Au NPs and was then incubated with RBD, Ab-F2, and Ab-F2 after RBD incubation. Fluorescence images are shown in Fig. 4B. The fluorescence intensity (Fig. 4C) and spectrum (Fig. 4F) associated with NB4E9-C were also consistent with those of NB1D6-C. The Au NPs successfully achieved the self-assembly of NBs and specific capture of RBD.

Thirty-six randomly selected biosensor chips were used to study the reproducibility of the Au NP- covered substrates before biological functionalization (Fig. 5A and D). Thirty-six biosensor chips were placed in a homemade 36-well plate to collect LSPR spectra, as shown in Fig. 5A. There is almost no significant difference in the LSPR spectral peak positions between slices, which indicates good slice-to-slice uniformity and reproducibility of the Au NP- covered substrate. The relative standard deviation (RSD) is as low as 0.21%. At the same time, the reproducibility of the chip test results after the self-assembly of NB1D6-C and NB4E9-C and the specific capture of RBD were investigated (Fig. 5B–F). Fig. 5B and C show the spectra of the Au NP- covered substrates after the self-assembled NB1D6-C, NB4E9-C, and specific capture of 1 μg/mL RBD, respectively, for 15 tests. The Au NP- covered substrates showed wavelength shifts after the self-assembled NBs and the specific capture of 1 μg/mL RBD. There was almost no significant difference in the LSPR spectral peak positions for the 15 tests, which indicated that the test results of self-assembled NB1D6-C, NB4E9-C, and RBD-specific capture substrates have good repeatability. Therefore, this immunoassay protocol can be used to further test the SARS-CoV-2 spike RBD.

3.4. Measurement and analysis of single NB biosensor

The excellent specificity of biosensors is one of the necessary conditions for achieving high sensitivity and reliable sensing. In addition to target analytes, other proteins may also non-specifically adsorb onto the surface of immune substrates. The target protein and other interfering protein solutions, including PBS, BSA, AFP, CEA, IgG, and CA15–3, were incubated on the immune substrates after NB self-assembly. The interfering protein solution showed a small non-specific adsorption on the two NB immune substrates. In contrast, the target protein at a concentration much lower than that of the interfering protein showed strong specific interactions with the two NB immune substrates (Fig. 6A and D). The results showed that the biosensors constructed using the two NBs had reasonable specificity and selectivity for the target antigen. Next, we exposed the two constructed NB biosensors to SARS-CoV-2 spike RBD at concentrations ranging from 0.1 to 10,000 ng/mL to verify the accuracy and reliability of the biosensor (Fig. 6B and E). The response of the biosensor (Δλ) generated by SARS-CoV-2 spike RBD of 0.1–10,000 ng/mL is related to the concentration (RBD) and can be calibrated with the Hill equation, which is the most commonly used to describe antigen–antibody interactions [44,45]:

$$\Delta\lambda = \frac{\Delta\lambda_{max} \times [RBD]}{k + [RBD]}$$

where, $\Delta\lambda_{max}$ is the maximum wavelength shift of the biosensor and k is the antibody–antigen affinity constant. According to the best-fitting results, the biosensor response based on NB1D6 are $\Delta\lambda_{max} = 3.02 \pm 0.14$ nm and $k = 44.77 \pm 9.03$ ng/mL. The biosensor response based on NB4E9 are $\Delta\lambda_{max} = 2.57 \pm 0.34$ nm and $k = 13.84 \pm 6.70$ ng/mL. At the same time, the wavelength shifts of the NB1D6-based biosensor in the range of 1–200 ng/mL increased continuously with the increase in the SARS-CoV-2 spike RBD. A strong linear relationship was observed (Fig. 6C). Similarly, the wavelength shift generated by the NB4E9-based

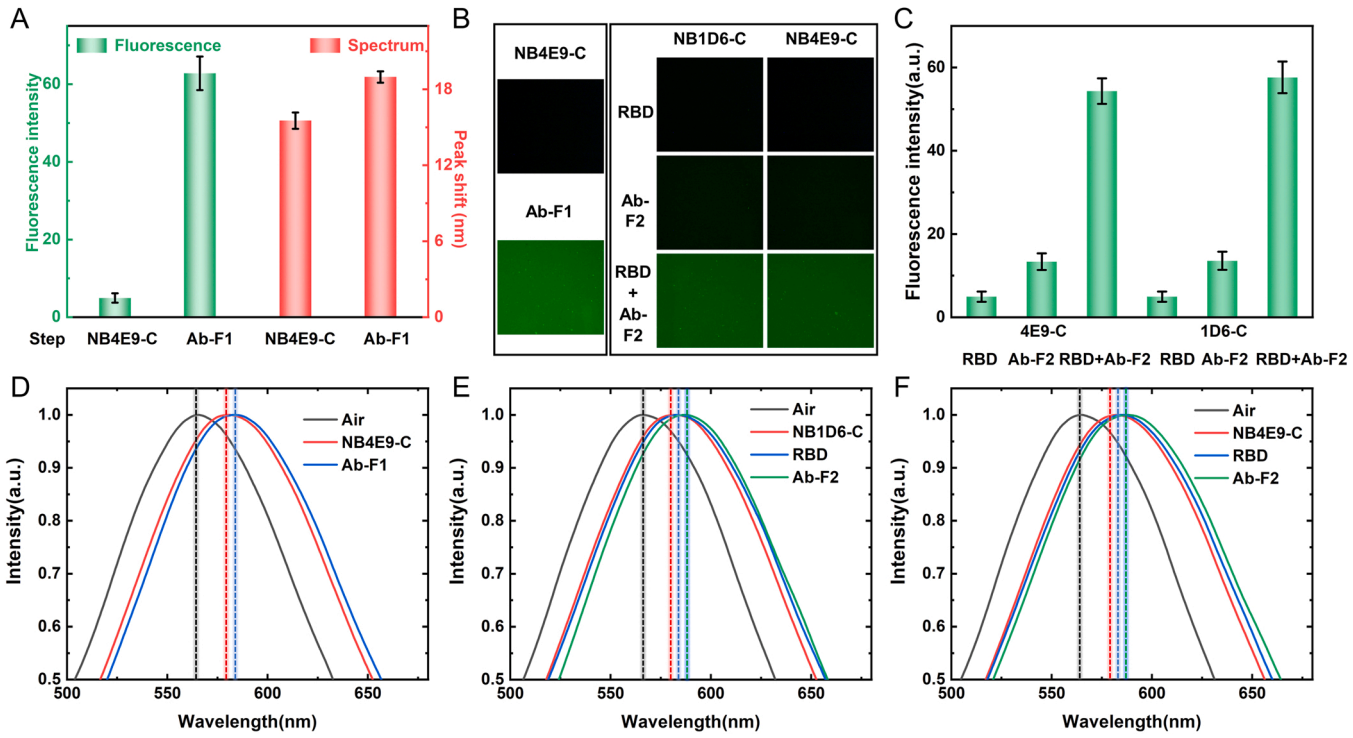

Fig. 4. Fluorescent characterization of immune sensing strategies. (A) The calculated fluorescence intensity and LSPR spectral wavelength shift of the Au NP-covered substrates after incubation in NB4E9-C and Ab-F1. (B) Fluorescence micrographs of NB4E9-C self-assembled Au NP-covered substrates and Ab-F1 incubated immune substrates (left box). Fluorescence micrographs of NB1D6-C and NB4E9-C self-assembled immune substrates incubated with RBD, Ab-F2, and Ab-F2 after RBD, respectively (right box). (C) The calculated fluorescence intensity of NB1D6-C and NB4E9-C self-assembled immune substrates incubated with RBD, Ab-F2, and RBD after Ab-F2, respectively. (D) LSPR spectra of Au NP-covered substrates after the initial (black), NB4E9-C incubation (red), and RBD incubation (blue). (E) LSPR spectra of Au NP-covered substrates after the initial (black), NB1D6-C incubation (red), RBD incubation (blue), and Ab-F2 incubation (green). (F) LSPR spectra of Au NP-covered substrates after the initial (black), NB4E9-C incubation (red), RBD incubation (blue), and Ab-F2 incubation (green).

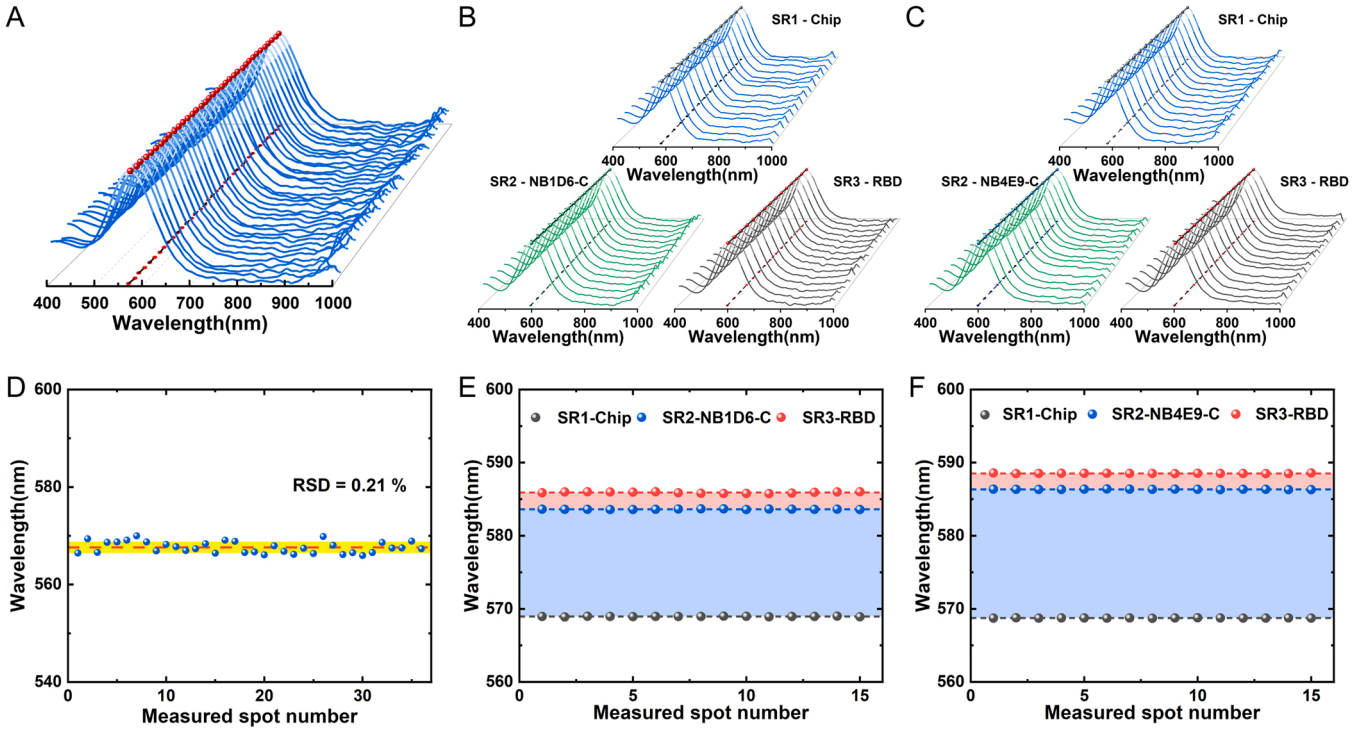

Fig. 5. Reproducible characterization of immune substrates. (A) LSPR spectra of 36 Au NP-covered substrates. The red balls represent the peak wavelength of the corresponding spectra. LSPR spectra of 15 tests during the functionalization of immune substrates constructed with NB1D6-C (B) and NB4E9-C (C): the initial (blue), NB self-assembly (green), and antigen capture (gray). (D) LSPR spectra peak positions of 36 Au NP-covered substrates. Peak positions of 15 tests during the functionalization of immune substrates constructed with NB1D6-C (E) and NB4E9-C (F): the initial (gray), NB self-assembly (blue), antigen capture (red).

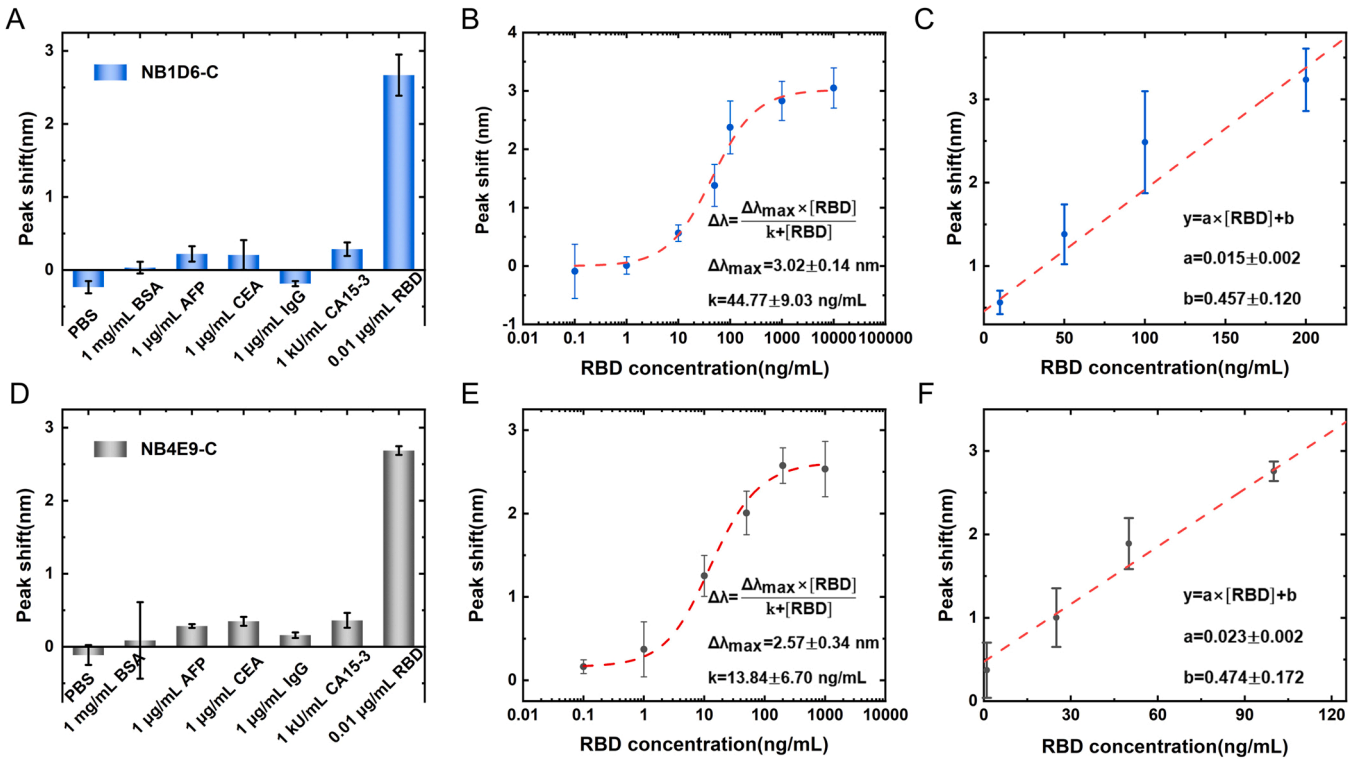

Fig. 6. Specificity and accuracy of biosensors constructed by the single NB. Responses (LSPR spectral wavelength shift) of biosensors constructed by NB1D6-C (A) and NB4E9-C (D) to different solutions: PBS, 1 mg/mL BSA, 1 μg/mL AFP, 1 μg/mL CEA, 1 μg/mL IgG, 1 kU/mL CA15–3, and 0.01 μg/mL SARS-CoV-2 spike RBD. Responses of biosensors constructed by NB1D6-C (B) and NB4E9-C (E) to different concentrations of SARS-CoV-2 spike RBD. The red dashed line is the standard concentration fitted by the Hill equation. The linearity range between detect concentration and the response of biosensors constructed by NB1D6-C (C) and NB4E9-C (F) to the SARS-CoV-2 spike RBD. The dotted line is the standard concentration calculated by linear regression. Error bars denote the standard deviations ($n = 3$).

biosensor established a good linear relationship with the SARS-CoV-2 spike RBD concentration in the range of 0.1–100 ng/mL (Fig. 6F).

3.5. Measurement and clinical application potential of a mixed NBs biosensor

Biosensors constructed using the two NBs alone exhibited good selectivity and specificity. However, the two biosensors used two NBs that specifically bound to the RBD. Biosensors have different k values and exhibit different sensing capabilities. A lower value of k indicates a higher detection sensitivity and results in a steeper curve of the sensing response [23,46]. The biosensor constructed in an equal-ratio mixture of NB1D6 and NB4E9 also exhibited the same reasonable specificity and selectivity as biosensors constructed using a single nanobody (Fig. 7A and D). As shown in Fig. 7 A, a significant spectral wavelength shift was observed only at 0.01 μg/mL of SARS-CoV-2 spike RBD. Even at a concentration of 1 μg/mL, other interfering protein solutions produced negligible spectral wavelength shifts owing to non-specific adsorption. Likewise, the immune biosensor constructed by the mixed NBs was exposed to SARS-CoV-2 spike RBD at concentrations ranging from 0.01 to 10,000 ng/mL to verify the accuracy and reliability of the biosensor (Fig. 7B). According to the Hill equation, the sensor response based on mixed NB1D6 and NB4E9 are $\Delta\lambda_{max} = 3.27 \pm 0.16$ nm and $k = 10.72 \pm 2.92$ ng/mL. The mixed NBs biosensor exhibited the most significant wavelength shift and covered the largest concentration range (Fig. 7E). The response parameters of the three immune biosensors based on the two NBs, are listed in Table S2. The biosensor constructed with the mixed NBs had the lowest k value. The wavelength shifts of the biosensor in the concentration range of 0.01–50 ng/mL SARS-CoV-2 spike RBD established a linear relationship, which lowered the measurable response concentration of the sensor. For the detection of the SARS-CoV-2 spike RBD, the minimum detection concentration of the sensor constructed by a single NB is similar to that of the sensor constructed by a single traditional antibody in the literature [23], namely 0.1 ng/mL. The biosensor constructed by mixing two NBs enhanced the detection sensitivity of the SARS-CoV-2 spike RBD, extending the minimum detection concentration to 0.01 ng/mL. Two non-competitively binding NB1D6 and NB4E9 proteins achieved more protein capture through mixed immobilization, enhancing the sensitivity of the sensor. The direct immobilization of more NBs (non-competing binding sites, uniform size, and exposed binding sites) may have the potential to increase detection sensitivity, but the balance of increased sensitivity, difficulty, and cost needs to be considered. Therefore, the proposed mixed NBs biosensor has more sensing response parameters and is the most promising candidate for clinical application among the three proposed sensors. Furthermore, different concentrations of target antigens in serum were used for immunoassays to simulate a real immunoassay environment. Sensing responses generated by the SARS-CoV-2 spike RBD at four concentrations (1, 25, 100, and 1000 ng/mL) were slightly higher in the serum environment (blue bars) than in the buffer environment (red bars). Non-specific adsorption of various impurities and small molecules present in serum samples may produce these slight differences, which can be ignored. In this experiment, the biosensor constructed using mixed NBs successfully extended the test concentration to a lower concentration, further improving the LSPR sensing sensitivity of biomodification rather than nanostructures. These results suggest that the proposed mixed NB-based biosensor has good potential for use in serum immunoassays.

4. Conclusions

A method has been developed to enable label-free quantification of the SARS-CoV-2 spike RBD in serum based on the direct immobilization of two engineered NBs biosensors. The metal nanostructures of the

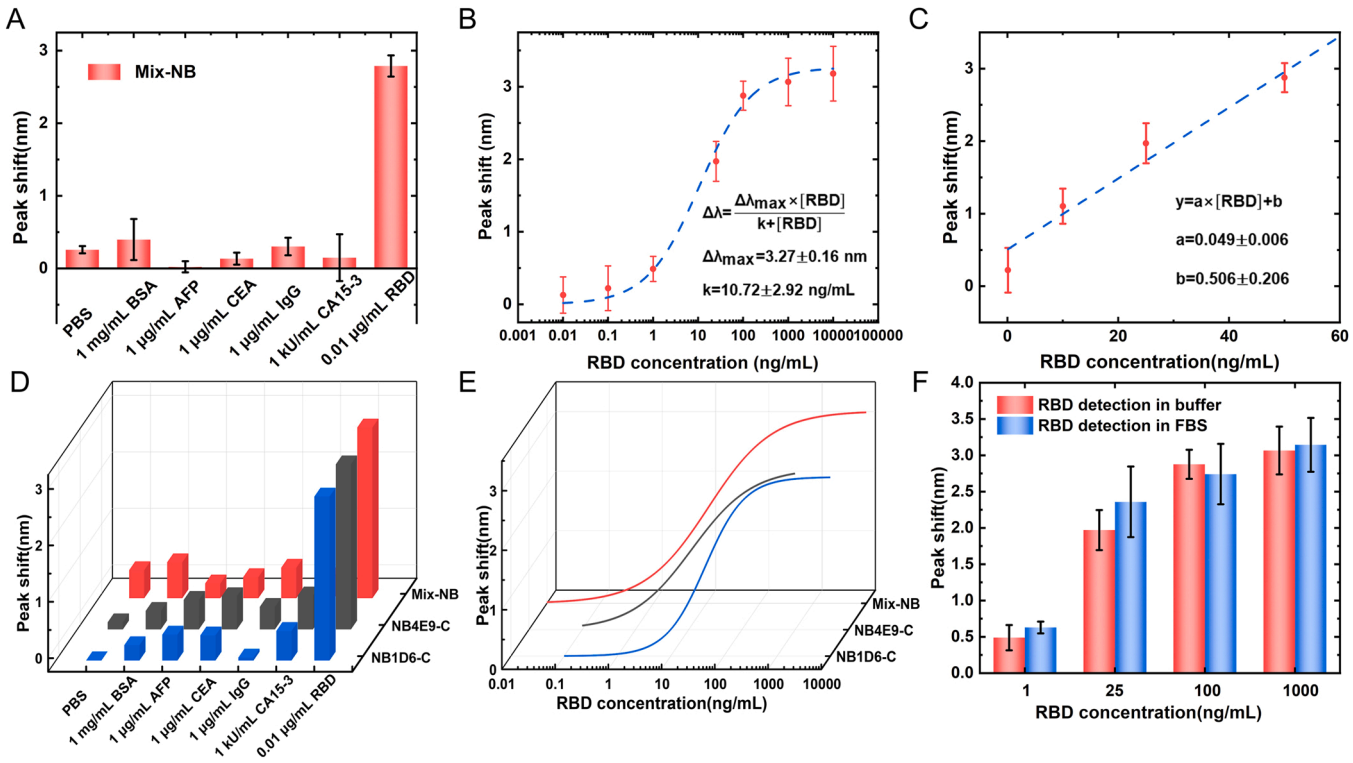

Fig. 7. Specificity, accuracy, and clinical potential of mixed NBs biosensors. (A). Responses (LSPR spectral wavelength shift) of mixed NBs biosensors to different solutions: PBS, 1 mg/mL BSA, 1 μg/mL AFP, 1 μg/mL CEA, 1 μg/mL IgG, 1 kU/mL CA15–3, and 0.01 μg/mL SARS-CoV-2 spike RBD. (B) Responses of mixed NBs biosensors to different concentrations of SARS-CoV-2 spike RBD. The red dashed line is the standard concentration fitted by the Hill equation. (C) The linearity range between detect concentration and the response of mixed NBs biosensors to the SARS-CoV-2 spike RBD. The dotted line is the standard concentration calculated by linear regression. (D) Specificity of biosensors constructed by NB1D6-C (blue), NB4E9-C (black), and mixed NBs (red). (E) Calibration curves of biosensors constructed by NB1D6-C (blue), NB4E9-C (black), and mixed NBs (red). (F) Responses of the mixed NBs biosensors to different concentrations of SARS-CoV-2 spike RBD in Tris-NaCl buffer (red) and serum (blue). Error bars denote the standard deviations ($n = 3$).

immune substrate have been fabricated using an optimized Au evaporation-annealing process on the FTO substrate. NBs with high affinity and specificity were selected as immune substances to capture the SARS-CoV-2 spike RBD. A sensing strategy for the direct immobilization of NBs has been proposed and its feasibility has been verified by immunofluorescence. The entire fabrication process and immune scheme of biosensors are straightforward, convenient, inexpensive, and have the potential for large-scale production. The mixed NBs biosensor successfully extended the sensing detection range with the lowest detection linear concentration (as low as 0.01 ng/mL, demonstrating the specificity of the developed nanoplasmonic biosensor. Overall, the proposed sensor has the potential for direct and sensitive screening of COVID-19 infections. In addition, the NB immobilization strategy and the mixed NBs enhanced the sensitivity strategy provided by the developed nanoplasmonic biosensor, which can be widely used in various biosensing methods to achieve accessible, highly sensitive, and highly specific quantitative detection of target protein concentration.

CRediT authorship contribution statement

Zhengtai Ma: Investigation, Validation, Methodology, Data curation, Formal analysis, Visualization, Writing – original draft, Writing – review & editing. **Zengchao Sun:** Resources, Visualization, Writing – review & editing. **Xiaoqing Lv:** Methodology, Writing – review & editing. **Hongda Chen:** Project administration, Supervision. **Yong Geng:** Resources, Methodology, Writing – review & editing, Supervision. **Zhaoxin Geng:** Conceptualization, Investigation, Validation, Methodology, Visualization, Writing – review & editing, Project administration, Supervision.

Declaration of Competing Interest

The authors declare that they have no known competing financial interests or personal relationships that could have appeared to influence the work reported in this paper.

Data availability

Data will be made available on request.

Acknowledgments

This work was supported by the National Natural Science Foundation of China (62274191, 61905293, and 62075211), the Natural Science Foundation of Beijing (4232075), Young and Middle-aged Talents Program of the State Ethnic Affairs Commission (2019), and the National Natural Science Foundation of China Youth Science Foundation Project (62004192).

Appendix A. Supporting information

Supplementary data associated with this article can be found in the online version at doi:10.1016/j.snb.2023.133575.

References

[1] D. Egger, E. Miguel, S.S. Warren, A. Shenoy, E. Collins, D. Karlan, D. Parkerson, A. M. Mobarak, G. Fink, C. Udry, M. Walker, J. Haushofer, M. Larreboure, S. Athey, P. Lopez-Pena, S. Benhachmi, M. Humphreys, L. Udry, N.F. Meriggi, A. Wabwire, C. A. Davis, U.J. Pape, T. Graff, M. Voors, C. Nekesa, C. Vernot, Falling living

standards during the COVID-19 crisis: Quantitative evidence from nine developing countries, Sci. Adv. 7 (2021), eabe0997, https://doi.org/10.1126/sciadv.abe0997.
[2] G.-u Kim, M.-J. Kim, S.H. Ra, J. Lee, S. Bae, J. Jung, S.-H. Kim, Clinical characteristics of asymptomatic and symptomatic patients with mild COVID-19, Clin. Micro Infec. 26 (2020) 948.e1–948.e3, https://doi.org/10.1016/j.cmi.2020.04.040.
[3] S. Pei, T.K. Yamana, S. Kandula, M. Galanti, J. Shaman, Burden and characteristics of COVID-19 in the United States during 2020, Nature 598 (2021) 338–341, https://doi.org/10.1038/s41586-021-03914-4.
[4] R. Rose-Redwood, R. Kitchin, E. Apostolopoulou, L. Rickards, T. Blackman, J. Crampton, U. Rossi, M. Buckley, Geographies of the COVID-19 pandemic, Dialog-. Hum. Geogr. 10 (2020) 97–106, https://doi.org/10.1177/2043820620936050.
[5] M. Yüce, E. Filiztekin, K.G. Özkaya, COVID-19 diagnosis —A review of current methods, Biosens. Bioelectron. 172 (2021), 112752, https://doi.org/10.1016/j.bios.2020.112752.
[6] J. Chen, R. Wang, M. Wang, G.-W. Wei, Mutations strengthened SARS-CoV-2 infectivity, J. Mol. Biol. 432 (2020) 5212–5226, https://doi.org/10.1016/j.jmb.2020.07.009.
[7] R. Wang, J. Chen, K. Gao, Y. Hozumi, C. Yin, G.-W. Wei, Analysis of SARS-CoV-2 mutations in the United States suggests presence of four substrains and novel variants, Commun. Biol. 4 (2021) 228, https://doi.org/10.1038/s42003-021-01754-6.
[8] Y. Wang, R. Chen, F. Hu, Y. Lan, Z. Yang, C. Zhan, J. Shi, X. Deng, M. Jiang, S. Zhong, B. Liao, K. Deng, J. Tang, L. Guo, M. Jiang, Q. Fan, M. Li, J. Liu, Y. Shi, X. Deng, X. Xiao, M. Kang, Y. Li, W. Guan, Y. Li, S. Li, F. Li, N. Zhong, X. Tang, Transmission, viral kinetics and clinical characteristics of the emergent SARS-CoV-2 Delta VOC in Guangzhou, China, eClinicalMedicine 40 (2021), 101129, https://doi.org/10.1016/j.eclinm.2021.101129.
[9] D. Wang, B. Hu, C. Hu, F. Zhu, X. Liu, J. Zhang, B. Wang, H. Xiang, Z. Cheng, Y. Xiong, Y. Zhao, Y. Li, X. Wang, Z. Peng, Clinical Characteristics of 138 Hospitalized Patients With 2019 Novel Coronavirus–Infected Pneumonia in Wuhan, China, JAMA 323 (2020) 1061, https://doi.org/10.1001/jama.2020.1585.
[10] N. Zhang, L. Wang, X. Deng, R. Liang, M. Su, C. He, L. Hu, Y. Su, J. Ren, F. Yu, L. Du, S. Jiang, Recent advances in the detection of respiratory virus infection in humans, J. Med. Virol. 92 (2020) 408–417, https://doi.org/10.1002/jmv.25674.
[11] O. Calvo-Lozano, M. Sierra, M. Soler, M.C. Estévez, L. Chiscano-Camón, A. Ruiz-Sanmartin, J.C. Ruiz-Rodriguez, R. Ferrer, J.J. González-López, J. Esperalba, C. Fernández-Naval, L. Bueno, R. López-Aladid, A. Torres, L. Fernández-Barat, S. Attoumani, R. Charrel, B. Coutard, L.M. Lechuga, Label-Free Plasmonic Biosensor for Rapid, Quantitative, and Highly Sensitive COVID-19 Serology: Implementation and Clinical Validation, Anal. Chem. 94 (2022) 975–984, https://doi.org/10.1021/acs.analchem.1c03850.
[12] T. Nolan, R.E. Hands, S.A. Bustin, Quantification of mRNA using real-time RT-PCR, Nat. Protoc. 1 (2006) 1559–1582, https://doi.org/10.1038/nprot.2006.236.
[13] F. Krammer, V. Simon, Serology assays to manage COVID-19, Science 368 (2020) 1060–1061, https://doi.org/10.1126/science.abc1227.
[14] Z. Li, Y. Yi, X. Luo, N. Xiong, Y. Liu, S. Li, R. Sun, Y. Wang, B. Hu, W. Chen, Y. Zhang, J. Wang, B. Huang, Y. Lin, J. Yang, W. Cai, X. Wang, J. Cheng, Z. Chen, K. Sun, W. Pan, Z. Zhan, L. Chen, F. Ye, Development and clinical application of a rapid IgM-IgG combined antibody test for SARS-CoV-2 infection diagnosis, J. Med. Virol. 92 (2020) 1518–1524, https://doi.org/10.1002/jmv.25727.
[15] F. Cui, H.S. Zhou, Diagnostic methods and potential portable biosensors for coronavirus disease 2019, Biosens. Bioelectron. 165 (2020), 112349, https://doi.org/10.1016/j.bios.2020.112349.
[16] S.A. Jadhav, P. Biji, M.K. Panthalingal, C. Murali Krishna, S. Rajkumar, D.S. Joshi, N. Sundaram, Development of integrated microfluidic platform coupled with Surface-enhanced Raman Spectroscopy for diagnosis of COVID-19, Med. Hypotheses 146 (2021), 110356, https://doi.org/10.1016/j.mehy.2020.110356.
[17] M. Zhang, X. Li, J. Pan, Y. Zhang, L. Zhang, C. Wang, X. Yan, X. Liu, G. Lu, Ultrasensitive detection of SARS-CoV-2 spike protein in untreated saliva using SERS-based biosensor, Biosens. Bioelectron. 190 (2021), 113421, https://doi.org/10.1016/j.bios.2021.113421.
[18] S.M. Sheta, S.M. El-Sheikh, Nanomaterials and metal-organic frameworks for biosensing applications of mutations of the emerging viruses, Anal. Biochem. 648 (2022), 114680, https://doi.org/10.1016/j.ab.2022.114680.
[19] D.M. El-Sherif, M. Abouzid, M.S. Gaballah, A.A. Ahmed, M. Adeel, S.M. Sheta, New approach in SARS-CoV-2 surveillance using biosensor technology: a review, Environ. Sci. Pollut. Res. 29 (2022) 1677–1695, https://doi.org/10.1007/s11356-021-17096-z.
[20] R. Funari, H. Fukuyama, A.Q. Shen, Nanoplasmonic multiplex biosensing for COVID-19 vaccines, Biosens. Bioelectron. 208 (2022), 114193, https://doi.org/10.1016/j.bios.2022.114193.
[21] Y. Yang, J. Murray, J. Haverstick, R.A. Tripp, Y. Zhao, Silver nanotriangle array based LSPR sensor for rapid coronavirus detection, Sens. Actuators B: Chem. 359 (2022), 131604, https://doi.org/10.1016/j.snb.2022.131604.
[22] N. Bhalla, A.F. Payam, A. Morelli, P.K. Sharma, R. Johnson, A. Thomson, P. Jolly, F. Canfarotta, Nanoplasmonic biosensor for rapid detection of multiple viral variants in human serum, Sens. Actuators B: Chem. 365 (2022), 131906, https://doi.org/10.1016/j.snb.2022.131906.
[23] R. Funari, K.-Y. Chu, A.Q. Shen, Detection of antibodies against SARS-CoV-2 spike protein by gold nanospikes in an opto-microfluidic chip, Biosens. Bioelectron. 169 (2020), 112578, https://doi.org/10.1016/j.bios.2020.112578.
[24] L. Huang, Y. Li, C. Luo, Y. Chen, N. Touil, H.-E. Annaz, S. Zeng, T. Dang, J. Liang, W. Hu, H. Xu, J. Tu, L. Wang, Y. Shen, G.L. Liu, Novel nanostructure-coupled biosensor platform for one-step high-throughput quantification of serum neutralizing antibody after COVID-19 vaccination, Biosens. Bioelectron. 199 (2022), 113868, https://doi.org/10.1016/j.bios.2021.113868.
[25] L. Hanke, L. Vidakovics Perez, D.J. Sheward, H. Das, T. Schulte, A. Moliner-Morro, M. Corcoran, A. Achour, G.B. Karlsson Hedestam, B.M. Hällberg, B. Murrell, G. M. McInerney, An alpaca nanobody neutralizes SARS-CoV-2 by blocking receptor interaction, Nat. Commun. 11 (2020) 4420, https://doi.org/10.1038/s41467-020-18174-5.
[26] Z. Shi, X. Li, L. Wang, Z. Sun, H. Zhang, X. Chen, Q. Cui, H. Qiao, Z. Lan, X. Zhang, X. Li, L. Li, J. Xu, R. Gong, C. Fan, Y. Geng, Structural basis of nanobodies neutralizing SARS-CoV-2 variants, 707-720.e5, Structure 30 (2022), https://doi.org/10.1016/j.str.2022.02.011.
[27] Z. Sun, L. Wang, X. Li, C. Fan, J. Xu, Z. Shi, H. Qiao, Z. Lan, X. Zhang, L. Li, X. Zhou, Y. Geng, An extended conformation of SARS-CoV-2 main protease reveals allosteric targets, Proc. Natl. Acad. Sci. U. S. A. 119 (2022), e2120913119, https://doi.org/10.1073/pnas.2120913119.
[28] M.A. de Beer, B.N.G. Giepmans, Nanobody-based probes for subcellular protein identification and visualization, Front. Cell. Neurosci. 14 (2020), 573278, https://doi.org/10.3389/fncel.2020.573278.
[29] H. Farrants, M. Tarnawski, T.G. Müller, S. Otsuka, J. Hiblot, B. Koch, M. Kueblbeck, H.-G. Kräusslich, J. Ellenberg, K. Johnsson, Chemogenetic control of nanobodies, Nat. Methods 17 (2020) 279–282, https://doi.org/10.1038/s41592-020-0746-7.
[30] Y. Yu, J. Li, X. Zhu, X. Tang, Y. Bao, X. Sun, Y. Huang, F. Tian, X. Liu, L. Yang, Humanized CD7 nanobody-based immunotoxins exhibit promising anti-T-cell acute lymphoblastic leukemia potential, IJN 12 (2017) 1969–1983, https://doi.org/10.2147/IJN.S127575.
[31] G. Longobucco, G. Fasano, M. Zharnikov, L. Bergamini, S. Corni, M.A. Rampi, High stability and sensitivity of gold nano-islands for localized surface plasmon spectroscopy: Role of solvent viscosity and morphology, Sens. Actuators B: Chem. 191 (2014) 356–363, https://doi.org/10.1016/j.snb.2013.09.026.
[32] P. Wang, R.E. Ionescu, Glucose sensing on reproducible and tunable plasmonic nanostructures formed on annealed coverslips coated with thin layers of gold and indium tin oxide, Sens. Actuators A: Phys. 318 (2021), 112510, https://doi.org/10.1016/j.sna.2020.112510.
[33] G. Mie, Beiträge zur Optik trüber Medien, speziell kolloidaler Metallösungen, Ann. Phys. 330 (1908) 377–445, https://doi.org/10.1002/andp.19083300302.
[34] J. Cao, T. Sun, K.T.V. Grattan, Gold nanorod-based localized surface plasmon resonance biosensors: A review, Sens. Actuators B: Chem. 195 (2014) 332–351, https://doi.org/10.1016/j.snb.2014.01.056.
[35] H. Chen, X. Kou, Z. Yang, W. Ni, J. Wang, Shape- and Size-Dependent Refractive Index Sensitivity of Gold Nanoparticles, Langmuir 24 (2008) 5233–5237, https://doi.org/10.1021/la800305j.
[36] S. Kaushal, S.S. Nanda, S. Samal, D.K. Yi, Strategies for the Development of Metallic-Nanoparticle-Based Label-Free Biosensors and Their Biomedical Applications, ChemBioChem 21 (2020) 576–600, https://doi.org/10.1002/cbic.201900566.
[37] S. Muyldermans, Nanobodies: natural single-domain antibodies, Annu. Rev. Biochem. 82 (2013) 775–797, https://doi.org/10.1146/annurev-biochem-063011-092449.
[38] J. Xu, K. Xu, S. Jung, A. Conte, J. Lieberman, F. Muecksch, J.C.C. Lorenzi, S. Park, F. Schmidt, Z. Wang, Y. Huang, Y. Luo, M.S. Nair, P. Wang, J.E. Schulz, L. Tessarollo, T. Bylund, G.-Y. Chuang, A.S. Olia, T. Stephens, I.-T. Teng, Y. Tsybovsky, T. Zhou, V. Munster, D.D. Ho, T. Hatziioannou, P.D. Bieniasz, M. C. Nussenzweig, P.D. Kwong, R. Casellas, Nanobodies from camelid mice and llamas neutralize SARS-CoV-2 variants, Nature 595 (2021) 278–282, https://doi.org/10.1038/s41586-021-03676-z.
[39] D. Ta, W. Guedens, T. Vranken, K. Vanschoenbeek, E. Steen Redeker, L. Michiels, P. Adriaensens, Enhanced Biosensor Platforms for Detecting the Atherosclerotic Biomarker VCAM1 Based on Bioconjugation with Uniformly Oriented VCAM1-Targeting Nanobodies, Biosensors 6 (2016) 34, https://doi.org/10.3390/bios6030034.
[40] L. Xu, H. Cao, C. Huang, L. Jia, Oriented immobilization and quantitative analysis simultaneously realized in sandwich immunoassay via his-tagged nanobody, Molecules 24 (2019) 1890, https://doi.org/10.3390/molecules24101890.
[41] B. Simões, W.J. Guedens, C. Keene, K. Kubiak-Ossowska, P. Mulheran, A. M. Kotowska, D.J. Scurr, M.R. Alexander, A. Broisat, S. Johnson, S. Muyldermans, N. Devoogdt, P. Adriaensens, P.M. Mendes, Direct immobilization of engineered nanobodies on gold sensors, ACS Appl. Mater. Inter. 13 (2021) 17353–17360, https://doi.org/10.1021/acsami.1c02280.
[42] P. Bryant, G. Pozzati, A. Elofsson, Improved prediction of protein-protein interactions using AlphaFold2, Nat. Commun. 13 (2022) 1265, https://doi.org/10.1038/s41467-022-28865-w.
[43] T. Aderinwale, V. Bharadwaj, C. Christoffer, G. Terashi, Z. Zhang, R. Jahandideh, Y. Kagaya, D. Kihara, Real-time structure search and structure classification for AlphaFold protein models, Commun. Biol. 5 (2022) 316, https://doi.org/10.1038/s42003-022-03261-8.
[44] E.C. Hulme, M.A. Trevethick, Ligand binding assays at equilibrium: validation and interpretation: Equilibrium binding assays, Brit. J. Pharmacol. 161 (2010) 1219–1237, https://doi.org/10.1111/j.1476-5381.2009.00604.x.
[45] I. Pereiro, J.F. Cors, S. Pané, B.J. Nelson, G.V. Kaigala, Underpinning transport phenomena for the patterning of biomolecules, Chem. Soc. Rev. 48 (2019) 1236–1254, https://doi.org/10.1039/C8CS00852C.
[46] X. Chen, F. Lisi, P. Bakthavathsalam, G. Longatte, S. Hoque, R.D. Tilley, J. J. Gooding, Impact of the coverage of aptamers on a nanoparticle on the binding equilibrium and kinetics between aptamer and protein, ACS Sens. 6 (2021) 538–545, https://doi.org/10.1021/acssensors.0c02212.

Zhengtai Ma received the B.S. degree from College of Science, Minzu University of China, in 2019. Presently, he is pursuing the Ph.D. degree with the Institute of Semiconductors Chinese Academy of Sciences. His current research interest is nanophotonics biosensing.

Zengchao Sun received the M.S. degree from Shanghai Ocean University, in 2022. Presently, he is an assistant engineer at Shanghai Institute of Materia Medica, Chinese Academy of Sciences. His current research interest is structural biology and nanoantibodies.

Xiaoqing Lv received the Ph.D. degree from Institute of Semiconductors Chinese Academy of Sciences, in 2018. Presently, she is an assistant Research Fellow at Institute of Semiconductors Chinese Academy of Sciences. Her current research interests are exosome detection and silicon optical sensing.

Hongda Chen received the B.S., M.S., and Ph.D. degrees from the Tianjin University of China, in 1982, 1990, and 1996, respectively. He has been involved in the scientific research and teaching optoelectronics and microelectronics for many years. He is currently a Professor with the University of Chinese Academy of Sciences. His current research field includes novel optoelectronic devices, photonic crystal devices and optical integrated circuits, design of sub-micrometer high-speed IC and radio frequency circuit, system on chip, OEIC, the application in LAN of high-speed parallel optical transmission modules, and high-speed very short reach parallel optical transmission system. He is a member of the Optical Society of America, a Senior Member of the Chinese Institute of Electronics, and a member of the Semiconductor Committee of Beijing Electronic Academy.

Yong Geng received the Ph.D. degree from Institute of Biophysics, Chinese Academy of Sciences, in 2006. Presently, he is currently a Research Fellow with the Shanghai Institute of Materia Medica, Chinese Academy of Sciences. His current research interests are structural biology and nanobodies, study on the structure and function of cellular receptors, receptor drug action mechanism, and nanobody discovery based on receptor structure.

Zhaoxin Geng received the Ph.D. degree from Institute of Electronics, Chinese Academy of Sciences, in 2007. Presently, he is a Professor at School of Information Engineering, Minzu University of China. Meanwhile. He was a Postdoctoral Fellow at Institute of Semiconductor, Chinese Academy of Sciences from 2009 to 2013. His current research focuses on the Micro/Nanofluidics, Biosensor, applications of nanoplas- monics, localized surface plasmon resonance (LSPR), and wireless sensor networks (WSN).